Magic-zero and magic wavelengths of the Ca atom

Ru-Kui Zhang,[1,2] Jun Jiang,[1,*] Chen-Zhong Dong,[1] and Yong-Bo Tang[2,†]

[1]*Key Laboratory of Atomic and Molecular Physics and Functional Materials of Gansu Province, College of Physics and Electronic Engineering, Northwest Normal University, Lanzhou 730070, People's Republic of China*

[2]*Physics Teaching and Experiment Center, Shenzhen Technology University, Shenzhen 518118, People's Republic of China*

(Received 3 April 2023; revised 14 June 2023; accepted 16 June 2023; published 7 July 2023)

The relativistic configuration interaction plus many-body perturbation (RCI + MBPT) method is utilized to calculate the wave functions, energy levels, and reduced $E1$ transition matrix elements of Ca atoms in detail. The static and dynamic polarizabilities of the $4s^2\ ^1S_0$, $4s4p\ ^1P_1$, and $4s4p\ ^3P_{0,1,2}$ states are determined by the sum-over-states method. A number of magic-zero wavelengths for the ground and $4s4p\ ^3P_0$ states, as well as magic wavelengths for the $4s^2\ ^1S_0 \rightarrow 4s4p\ ^3P_0$ and $4s^2\ ^1S_0 \rightarrow 4s4p\ ^3P_1$ transitions, are obtained. We suggest that the measurements of the magic-zero wavelengths of the $4s4p\ ^3P_0$ states can be used to determine oscillator strengths with high precision. In addition, the angle-dependent magic wavelengths of each magnetic sublevel transition of the $4s^2\ ^1S_0 \rightarrow 4s4p\ ^3P_1$ transition are provided, which are of particular interest for optical frequency measurements, Bose-Einstein condensate generation, and superradiant laser technology.

DOI: 10.1103/PhysRevA.108.012803

I. INTRODUCTION

The technique of manipulating atoms with lasers is widely used in high-precision measurements, including atomic clocks [1–5], atomic magnetometers [6–8], and atomic interferometers [9–12]. However, the accuracy of atomic parameter measurements can be affected by ac Stark shifts resulting from the interactions between laser fields and atoms. To address this issue, magic trapping for a specific transition is utilized, where the ac Stark shifts caused by the electric dipole interactions cancel out for the states involved. The laser wavelength used in this trapping is known as the magic wavelength [13,14].

In addition, the application of a trapping laser at a specific frequency can result in a zero ac Stark shift of an atomic state, which is referred to as the magic-zero (or tune-out) wavelength. High-precision measurements of the magic-zero wavelengths can be used to test the theory of atomic structure and determine atomic parameters with high accuracy [15–25]. For example, the transition matrix elements of $5s$-$6p_{1/2,3/2}$ in Rb atoms are determined with an accuracy of 10^{-3} by measuring the ac Stark shift around 421- and 423-nm magic-zero wavelengths [15]. The longest magic-zero wavelength of the ground state of the K atom is measured with an uncertainty of 1.5 pm [18], and the ratio of the line strengths $S_{4s\rightarrow 4p_{3/2}}/S_{4s\rightarrow 4p_{1/2}}$ is obtained with an accuracy of 0.05%. The measurement of the 413-nm magic-zero wavelength of the metastable $2\ ^3S_1$ state of helium is used to test the quantum electrodynamics effects [23,24]. The ratio of the $6s_{1/2} \rightarrow 6p_{1/2,3/2}$ transition matrix elements in Cs atoms is determined at the 10^{-4} level by measuring the magic-zero wavelength near 880 nm [25].

Ca is an important candidate in the field of precision measurement physics. Numerous studies have been focused on the ultracold Ca atoms [26–30], Bose-Einstein condensate (BEC) [31–38], optical frequency standards [39–44], and superradiant emission of atoms trapped in an optical cavity [45]. To conduct these experiments, detailed information about Ca atoms, including the static and dynamic polarizabilities, magic-zero wavelengths, and magic wavelengths, is highly required.

In theory, Zhou *et al.* [46] calculated some magic wavelengths for the transitions $4s4p\ ^3P_0 \rightarrow 4s4p\ ^3P_1$, $m_j = 0$ and $4s4p\ ^3P_1$, $m_j = 0 \rightarrow 4s4p\ ^3P_2$, $m_j = 0$ using the sum-over-states method. However, only 30 excited states were used in their calculations, where the transitions rates are collected from Ref. [42] and National Institute of Standards and Technology (NIST) tabulations [47] that are derived from spectrographic analysis of astrophysical data. Recently, Gogyan *et al.* [48] presented the magic wavelengths for the $4s^2\ ^1S_0 \rightarrow 4s4p\ ^3P_1$ transition and the magic-zero wavelengths for the $4s4p\ ^3P_1$, $m_j = 0$, state using Einstein coefficients that are the same as Zhou *et al.* [46]. The magic-zero wavelengths of the ground state of Ca were calculated by Cheng *et al.* [49] using a semiempirical method.

In this work, the wave functions, energy levels, reduced $E1$ transition matrix elements, and static and dynamic dipole polarizabilities for $4s^2\ ^1S_0$ and $4s4p\ ^3P_J$ states of Ca atoms are calculated using the relativistic configuration interaction plus many-body perturbation method. The magic-zero wavelengths of $4s^2\ ^1S_0$ and $4s4p\ ^3P_0$ states, as well as the magic wavelengths for $4s^2\ ^1S_0 \rightarrow 4s4p\ ^3P_{0,1}$ transitions, are determined. We also propose that measurements of these magic or magic-zero wavelengths can be used to extract the related reduced matrix elements. Atomic units are used throughout this paper unless stated otherwise.

*phyjiang@yeah.net
†tangyongbo@sztu.edu.cn

II. THEORY

A. RCI + MBPT Method

In this work, we obtain the wave function and energies of Ca atoms using the relativistic configuration interaction plus second-order many-body perturbation (RCI + MBPT) method that has been adopted widely into atomic structure property calculations [61–64]. The basic strategy of this method is to simplify a many-electron atomic or ionic system into a frozen core part and valence electron parts. The first step is to perform the Dirac-Fock (DF) calculation of the frozen core part to obtain all single-particle orbitals, which are then used to construct the configuration space. The core-valence and valence-valence correlations are considered by using a correlation potential from the second-order many-body perturbation calculation and the configuration interaction method, respectively.

For a divalent system, the Dirac-Hamiltonian equation can be expressed as

$$\left(\sum_{i}^{2} h_i + \sum_{i<j}^{2} V_{ij}\right)|\Psi(\pi JM)\rangle = E|\Psi(\pi JM)\rangle, \tag{1}$$

where h_i represents the one-particle Hamiltonian and is written as

$$h_i = c\alpha_i \cdot \mathbf{p}_i + (\beta_i - 1)c^2 + V_N(r_i) + V_{\text{core}}(r_i). \tag{2}$$

Here, α and β are the Dirac matrices, $\mathbf{p}_i$ is the momentum operator for the ith electron, and $V_N(r_i)$ is the Coulomb potential between the ith electron and the nucleus. V_{core} represents the interaction potential between the core electrons and a valence electron, which is approximated as a DF potential and a one-body correlation potential:

$$V_{\text{core}} = V_{\text{DF}} + \Sigma_1. \tag{3}$$

The two-particle interaction Hamiltonian is given by

$$V_{ij} = \frac{1}{r_{ij}} + \Sigma_2, \tag{4}$$

where the first term represents the electron-electron Coulomb interaction, and the second term represents the two-body correlation potential.

The wave function $|\Psi(\pi JM)\rangle$ of the system is described as a linear combination of the configuration-state wave functions with the same parity π, angular momentum J, and magnetic quantum number M, namely,

$$|\Psi(\pi JM)\rangle = \sum_{k\leqslant l} C_{kl}|\Phi_{kl}(\pi JM)\rangle, \tag{5}$$

where C_{kl} are the expansion coefficients. The configuration wave function is a single-determinant basis state constructed from single-electron orbitals:

$$|\Phi_{kl}(\pi JM)\rangle = \eta_{kl}\sum_{m_k,m_l}\langle j_k m_k, j_l m_l|JM\rangle a_k^\dagger a_l^\dagger|0\rangle. \tag{6}$$

The symmetry factor η_{kl} is defined as

$$\eta_{kl} = \begin{cases} \frac{\sqrt{2}}{2}, & k = l, \\ 1, & k \neq l. \end{cases} \tag{7}$$

TABLE I. Comparison of energy (in cm^{-1}) for some low-lying states of Ca atom.

State	Present	NIST [47]	Diff.
$4s^2\ ^1S_0$	−145169.1	−145057.8	0.08%
$4s5s\ ^1S_0$	−111930.5	−111740.5	0.17%
$4p^2\ ^3P_0$	−106997.2	−106640.2	0.33%
$4s6s\ ^1S_0$	−104705.1	−104367.3	0.32%
$4p^2\ ^1S_0$	−103648.1	−103271.5	0.36%
$4s4p\ ^3P_0^o$	−130024.9	−129899.9	0.10%
$4s5p\ ^3P_0^o$	−108771.9	−108510.1	0.24%
$3d4p\ ^3P_0^o$	−106426.3	−105724.4	0.66%
$4s6p\ ^3P_0^o$	−102778.8	−102542.9	0.23%
$4s7p\ ^3P_0^o$	−100330.4	−100102.1	0.23%
$3d4s\ ^3D_1$	−125322.2	−124722.4	0.48%
$4s5s\ ^3S_1$	−113718.2	−113518.3	0.18%
$4s4d\ ^3D_1$	−107553.2	−107309.6	0.23%
$4p^2\ ^3P_1$	−106950.7	−106593.0	0.34%
$4s6s\ ^3S_1$	−104802.1	−104583.5	0.21%
$4s5d\ ^3D_1$	−102555.3	−102314.8	0.24%
$4s7s\ ^3S_1$	−101301.1	−101077.0	0.22%
$4s6d\ ^3D_1$	−100258.7	−100008.7	0.25%
$4s8s\ ^3S_1$	−99545.4	−99319.1	0.23%
$4s7d\ ^3D_1$	−99042.6	−98755.8	0.29%
$4s4p\ ^3P_1^o$	−129972.8	−129847.7	0.10%
$4s4p\ ^1P_1^o$	−121722.3	−121405.5	0.26%
$4s5p\ ^3P_1^o$	−108765.6	−108503.0	0.24%
$4s5p\ ^1P_1^o$	−108623.1	−108326.2	0.27%
$3d4p\ ^3D_1^o$	−107718.1	−106865.4	0.80%
$3d4s\ ^3D_2$	−125307.7	−124708.5	0.48%
$3d4s\ ^1D_2$	−123674.3	−123208.1	0.38%
$4s4d\ ^1D_2$	−108061.1	−107759.5	0.28%
$4s4d\ ^3D_2$	−107549.5	−107305.9	0.23%
$4p^2\ ^3P_2$	−106865.4	−106506.2	0.34%
$4p^2\ ^1D_2$	−104813.2	−104337.9	0.46%
$4s5d\ ^3D_2$	−102553.5	−102313.1	0.24%
$4s5d\ ^1D_2$	−102532.9	−102138.7	0.39%
$3d^2\ ^3F_2$	−102454.0	−101582.9	0.86%
$4s6d\ ^1D_2$	−100365.1	−100067.9	0.30%
$4s4p\ ^3P_2^o$	−129868.1	−129741.8	0.10%
$3d4p\ ^3F_2^o$	−110053.4	−109327.3	0.66%
$3d4p\ ^1D_2^o$	−109952.7	−109222.4	0.67%
$4s5p\ ^3P_2^o$	−108745.0	−108482.7	0.24%
$3d4s\ ^3D_3$	−125285.1	−124686.8	0.48%
$4s4d\ ^3D_3$	−107543.8	−107300.3	0.23%
$4s5d\ ^3D_3$	−102550.6	−102310.4	0.23%
$3d^2\ ^3F_3$	−102517.8	−101568.7	0.93%
$4s6d\ ^3D_3$	−100393.0	−100005.4	0.39%

Substituting Eq. (5) into Eq. (1) and applying the variational principle, we can obtain a general eigenvalue equation. Solving this eigenvalue equation yields the energies and wave functions of the system, which can be used to evaluate various properties.

In the present work, we construct the one-body Σ_1 and two-body Σ_2 correlation potentials using a second-order many-body perturbation calculation in the Brillouin-Wigner variant. The matrix elements of the one-body and two-body correlation potentials have been given in Ref. [65].

TABLE II. Comparison of some reduced $E1$ matrix elements (in a.u.) for principal transitions of Ca. Numbers in parentheses represent the uncertainties in the last digits.

	$\langle i\|D\|n\rangle$			
Transition	Present	CI + MBPT	Others	Expt.
$4s^2\ ^1S_0 \to 4s4p\ ^1P_1$	4.932(15)	4.91(7) [50]	4.951 [51]	4.967(9) [52]
		4.892 [53]	4.94 [49]	4.99(4) [54]
		4.930 [55]		4.93(11) [56]
$4s^2\ ^1S_0 \to 4s4p\ ^3P_1$	0.034(3)	0.034(4) [50]		0.0357(4) [57]
		0.0323 [53]		0.0352(10) [58]
				0.03571(16) [59]
$4s^2\ ^1S_0 \to 4s5p\ ^1P_1$	0.030(2)			0.089[a] [47]
$4s^2\ ^1S_0 \to 4s5p\ ^3P_1$	0.008(1)			
$4s4p\ ^3P_0 \to 3d4s\ ^3D_1$	2.196(5)			
$4s4p\ ^3P_0 \to 4s4d\ ^3D_1$	2.473(6)			2.529[a] [47]
$4s4p\ ^3P_0 \to 4p^2\ \ ^3P_1$	2.622(6)			2.658[a] [47]
				2.642(66)[a] [60]
$4s4p\ ^3P_0 \to 4s5s\ ^3S_1$	1.767(4)			1.793[a] [47]
				1.766(53)[a] [60]
$4s4p\ ^3P_0 \to 4s6s\ ^3S_1$	0.496(5)			0.552[a] [47]
$4s4p\ ^3P_0 \to 4s7s\ ^3S_1$	0.275(23)			0.283[a] [47]
$4s4p\ ^3P_0 \to 4s5d\ ^3D_1$	1.177(98)			1.221[a] [47]
$4s4p\ ^3P_0 \to 4s6d\ ^3D_1$	0.743(97)			0.915[a] [47]
$4s4p\ ^3P_1 \to 3d4s\ ^3D_2$	3.294(78)			
$4s4p\ ^3P_1 \to 3d4s\ ^3D_1$	1.904(59)			
$4s4p\ ^3P_1 \to 4s4d\ ^3D_2$	3.714(88)			3.802[a] [47]
$4s4p\ ^3P_1 \to 4s5s\ ^3S_1$	3.066(72)			3.121[a] [47]
				3.046(76)[a] [60]
$4s4p\ ^3P_1 \to 4p^2\ ^3P_0$	2.640(62)			2.806[a] [47]
				2.609(65)[a] [60]
$4s4p\ ^3P_2 \to 3d4s\ ^3D_3$	4.508(60)			
$4s4p\ ^3P_2 \to 4s4d\ ^3D_3$	5.507(72)			5.139[a] [47]
$4s4p\ ^1P_1 \to 3d4s\ ^1D_2$	1.009(84)	1.2(3) [50]		
$4s4p\ ^1P_1 \to 4s5s\ ^3S_1$	0.041(3)	0.043(5) [50]		
$4s4p\ ^1P_1 \to 4p^2\ ^1D_2$	5.843(63)			5.743[a] [47]

[a]The experimental matrix element of Refs. [47,60] are derived from the absorbed oscillator strength using Eq. (12), in which the transition energies are from NIST tabulations [47].

Additionally, to minimize the omitted higher-order MBPT effects, we introduce a rescaling parameter ρ_κ and the one-body correlation potential Σ_1 is replaced by $\rho_\kappa \Sigma_1$. The rescaling parameter ρ_κ is tuned to reproduce the experimental energy of the lowest state for each angular quantum number κ of a monovalent atomic system. It should be noted that the calculation of the transition matrix elements should take into account the core polarization correction. Here, the core polarization correction was considered using the random phase approximation [66,67].

Similar to Refs. [68–70], we use the no-pair Dirac Hamiltonian as the starting point and treat both the Coulomb and the Breit interactions on an equal footing. The large and small components of the Dirac wave functions are expanded using the k-order B-spline basis. We use 50 B-spline bases of order $k = 13$ and the box size $R_{\max} = 240$. The partial waves are limited to $\ell_{\max} = 5$ and the lowest 39 orbitals sets of each partial wave are used to construct the configuration space. In the second-order many-body perturbation calculations, the summation is carried out over the entire basis set. The rescaling parameters are $\rho_{-1} = 0.913$, $\rho_1 = 0.953$, $\rho_{-2} = 0.955$, $\rho_2 = 0.950$, $\rho_{-3} = 0.951$, and $\rho_{\text{others}} = 1.0$, respectively.

B. Polarizabilities

The dynamic polarizability of an atomic state i can be written as [87–90]

$$\alpha_i(\omega) = \alpha_i^S(\omega) + \mathcal{A}\cos\theta_k \frac{M_{J_i}}{2J_i}\alpha_i^V(\omega) + \frac{3\cos^2\theta_p - 1}{2}\frac{3M_{J_i}^2 - J_i(J_i+1)}{J_i(2J_i-1)}\alpha_i^T(\omega), \quad (8)$$

where $\alpha_i^S(\omega)$, $\alpha_i^V(\omega)$, and $\alpha_i^T(\omega)$ are the scalar, vector, and tensor polarizabilities, respectively. M_{J_i} is the component of the total angular momentum J_i, and $\mathcal{A}$ represents the degree of polarization ($\mathcal{A} = 0$ is linearly polarized light, $\mathcal{A} = +1$ and -1 are the right-handed and left-handed circularly polarized light, respectively). θ_k is the angle between the wave vector $\hat{k}$ and the direction of the magnetic field (quantization axis $\hat{e}_z$), $\cos\theta_k = \hat{k}\cdot\hat{e}_z$, and θ_p refers to the direction of laser polarization (the polarization vector $\hat{\varepsilon}$) with respect to the $\hat{e}_z$ axis. Geometrically, θ_k and θ_p satisfy the relation $\cos^2\theta_k + \cos^2\theta_p \leqslant 1$. The more general geometric interpretation of θ_p

and θ_k has been discussed in detail in Refs. [88,91]. The scalar, vector, and tensor polarizabilities can be expressed as

$$\alpha_i^S(\omega) = \sum_n \frac{f_{\rm in}}{\varepsilon_{\rm in}^2 - \omega^2}, \tag{9}$$

$$\alpha_i^V(\omega) = -3\sqrt{\frac{(6J_i)(2J_i+1)}{J_i+1}} \sum_n (-1)^{J_i+J_n} \times \begin{Bmatrix} 1 & 1 & 1 \\ J_i & J_i & J_n \end{Bmatrix} \frac{\omega f_{\rm in}}{\varepsilon_{\rm in}} \frac{1}{\varepsilon_{\rm in}^2 - \omega^2}, \tag{10}$$

and

$$\alpha_i^T(\omega) = 6\left(\frac{5J_i(2J_i-1)(2J_i+1)}{6(J_i+1)(2J_i+3)}\right)^{1/2} \times \sum_n (-1)^{J_i+J_n} \begin{Bmatrix} 1 & 1 & 2 \\ J_i & J_i & J_n \end{Bmatrix} \frac{f_{\rm in}}{\varepsilon_{\rm in}^2 - \omega^2}, \tag{11}$$

where $\varepsilon_{\rm in} = E_n - E_i$ is excitation energy, The oscillator strength is expressed as

$$f_{\rm in} = \frac{2\varepsilon_{ni}\langle\Psi_n\|D\|\Psi_i\rangle^2}{3(2J_i+1)}. \tag{12}$$

$\langle\Psi_n\|D\|\Psi_i\rangle$ is the reduced $E1$ transition matrix element.

When the magnetic field is parallel to the wave vector $\hat{k}$, i.e., $\cos\theta_k = 1$ and $\cos^2\theta_p = 0$, Eq. (8) is simplified as

$$\alpha_i(\omega) = \alpha_i^S(\omega) + \mathcal{A}\frac{M_{J_i}}{2J_i}\alpha_i^V(\omega) - \frac{3M_{J_i}^2 - J_i(J_i+1)}{2J_i(2J_i-1)}\alpha_i^T(\omega), \tag{13}$$

and when the magnetic field is perpendicular to the wave vector $\hat{k}$, i.e., $\cos\theta_k = 0$, Eq. (8) is

$$\alpha_i(\omega) = \alpha_i^S(\omega) + \frac{3\cos^2\theta_p - 1}{2}\frac{3M_{J_i}^2 - J_i(J_i+1)}{J_i(2J_i-1)}\alpha_i^T(\omega). \tag{14}$$

The static polarizabilities can be obtained from the above equations by setting $\omega = 0$. The experimental transition energies are used and all of the intermediate states are included in our calculation of polarizabilities. For example, $N_{J^-=1} = 16\,499$ states ($-$ represents the odd parity) are used to evaluate the polarizability of the $4s^2\ ^1S_0$ state, and $N_{J^+=1} = 14\,424$ states ($+$ represents the even parity) are used to evaluate the polarizability of the $4s4p\ ^3P_0$ state.

III. RESULTS AND DISCUSSION

A. Energy levels and reduced $E1$ transition matrix elements

To test the correctness and reliability of our method, we made detailed comparisons of the energies and reduced matrix elements in Tables I and II with available experimental and theoretical information. As shown in Table I, the present RCI + MBPT results show excellent agreement with the NIST energies [47], with the differences less than 0.5% for most of the states. The only exception is for some $3d$-related states, where the difference is 0.5%–1%. From Table II, we find that, for the resonant transition $4s^2\ ^1S_0 \rightarrow 4s4p\ ^1P_1$, our result is in good agreement with the experimental [56] and theoretical results [49,50,55], with a difference of about 1%. For the transitions $4s4p\ ^1P_1 \rightarrow 3d4s\ ^1D_2$ and $4s4p\ ^1P_1 \rightarrow 4s5s\ ^3S_1$, which are important for the calculations of the polarizabilities for the $4s4p\ ^3P_1$ and $4s4p\ ^1P_1$ states, the present results agree well with the theoretical calculations of Ref. [50], with a difference of about 15%. There are no experimental results available for these transitions. For the transition of $4s4p\ ^3P_2 \rightarrow 4s4d\ ^3D_3$, the present result agrees with the experimental result [47], with a difference of about 10%. Particularly, for some transitions, the present results are in better agreement with the latest reported results [60]. The uncertainties of the present matrix elements given in the Table II are estimated using the same method as for Cs atoms in Ref. [92].

TABLE III. Comparison of the static scalar and tensor dipole polarizabilities (a.u.) of the $4s^2\ ^1S_0$, $4s4p\ ^1P_1$, and $4s4p\ ^3P_{0,1,2}$ states of the Ca atoms with available experimental and theoretical results. The core polarizability of 3.26 a.u. [71] is adopted in the present calculations.

Methods	α^S	α^T
	$4s^2\ ^1S_0$	
Present	159.43(97)	
Finite-field [72]	157	
ab initio [73]	154.7	
CPP [74]	156.0	
Semiempirical [75]	159.4	
RCCSD [76]	158.00	
CI + MBPT [77]	159.0	
CICP [49]	159.4	
CI [78]	159.4	
Expt. [79]	168.7(13.5)	
Expt. [80]	169(17)	
	$4s4p\ ^3P_0$	
Present	280.8(1.2)	
RMBPT [81]	290.3(1.5)	
TDGI [82]	276	
	$4s4p\ ^1P_1$	
Present	244.6(1.5)	−53.86(33)
CI [78]	242.4	−55.54
Expt. [83]		−54.7(1.2)
	$4s4p\ ^3P_1$	
Present	282.4(1.7)	13.32(8)
CI [78]		14.2
Expt. [84]		12.9(3.2)
Expt. [85]		10.54(6)
Expt. [86]		12.1(8)
	$4s4p\ ^3P_2$	
Present	286.2(1.8)	−27.26(16)

B. The static dipole polarizabilities of $4s^2\ ^1S_0$, $4s4p\ ^1P_1$, and $4s4p\ ^3P_J$ states

Table III lists the static scalar and tensor dipole polarizabilities of the $4s^2\ ^1S_0$, $4s4p\ ^1P_1$, and $4s4p\ ^3P_{0,1,2}$ states of Ca atoms. The present results are compared with available theoretical results [49,72–78,82,93] and experimental values [79,80,83–86,94]. For the ground state $4s^2\ ^1S_0$, our RCI + MBPT result of 159.43(97) a.u. is in excellent agreement with the semiempirical [75], configuration interaction plus core

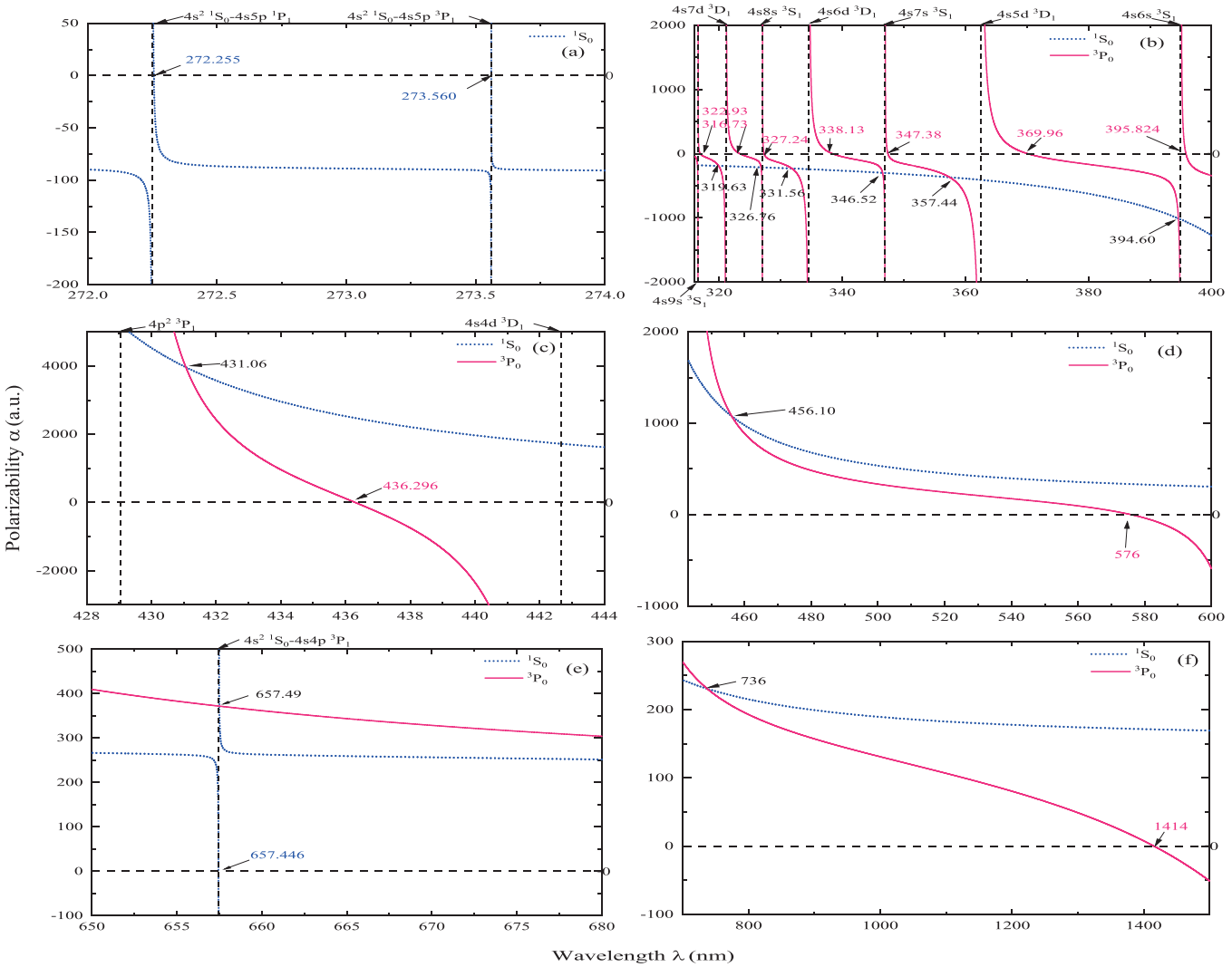

FIG. 1. The dynamical polarizabilities of $4s^2\ ^1S_0$ and $4s4p\ ^3P_0$ states. The vertical dashed lines indicate the position of the resonant transition. To facilitate the expression, only the upper states for resonances from the $4s4p\ ^3P_0$ state are given on the top of the figures. The magic-zero wavelength of a state is determined when the polarizability is zero, and the magic wavelength for a specific transition is located at the crossing points of polarizabilities for the states involved. They are all identified by arrows in this figure.

polarization (CICP) [49], and configuration interaction (CI) [78] calculations, with differences of no more than 0.05%, while the differences with core polarization potential (CPP) [74] calculations and the relativistic single coupled-cluster approach with single-double excitations (RCCSD) [76] are no more than 2%. Moreover, our result is also within the experimental error bar [79,80,94]. For the $4s4p\ ^3P_0$ state, the present scalar polarizability of 280.8 a.u. lies between the relativistic many-body perturbation theory (RMBPT) [81] and the time-dependent gauge invariant (TDGI) results [82]. For the $4s4p\ ^1P_1$ state, our polarizability is in good agreement with the experimental value [83] and the theoretical result [78], with differences of no more than 3% for both the scalar and the tensor polarizabilities. For the $4s4p\ ^3P_1$ state, our tensor polarizability is within the uncertainty range of the experimental result [84] and agrees well with the CI result [78]. There are no experimental or theoretical results available for the scalar polarizabilities of the $4s4p\ ^3P_1$ and $4s4p\ ^3P_2$ states.

C. The dynamic dipole polarizabilities of $4s^2\ ^1S_0$ and $4s4p\ ^3P_0$ states

Figure 1 shows the dynamic polarizabilities of the $4s^2\ ^1S_0$ and $4s4p\ ^3P_0$ states. For the ground state $4s^2\ ^1S_0$, three magic-zero wavelengths are found at 272.255, 273.560, and 657.446 nm [see the Figs. 1(a) and 1(e)], respectively. Table IV lists the breakdown of the contributions to the dynamic polarizabilities at these three magic-zero wavelengths, as well as the magic-zero wavelengths calculated using a semiempirical method [49]. The present results are in excellent agreement with the calculations of the semiempirical method [49]. As noted in Ref. [49], high-precision measurements of these three magic-zero wavelengths can effectively determine the values of $f_{4s^2\ ^1S_0\rightarrow 4s4p\ ^1P_1}/f_{4s^2\ ^1S_0\rightarrow 4s5p\ ^1P_1}$, $f_{4s^2\ ^1S_0\rightarrow 4s4p\ ^1P_1}/f_{4s^2\ ^1S_0\rightarrow 4s5p\ ^3P_1}$, and $f_{4s^2\ ^1S_0\rightarrow 4s4p\ ^1P_1}/f_{4s^2\ ^1S_0\rightarrow 4s4p\ ^3P_1}$.

There are ten magic-zero wavelengths in the range of 315 to 1500 nm for the $4s4p\ ^3P_0$ state, as listed in Table V.

TABLE IV. Magic-zero wavelengths (in nm) of the $4s^2\ ^1S_0$ state and breakdowns of the contributions to the dynamic polarizabilities (a.u.).

λ_{zero} (nm)	657.446	273.560	272.255
Ref. [49]	657.446	273.563	272.287
$4s4p\ ^1P_1$	256.557	−108.352	−106.591
$4s4p\ ^3P_1$	−269.936	−0.0023	−0.0023
$4s6p\ ^1P_1$	1.900	7.558	7.828
$4s5p\ ^1P_1$	0.042	0.367	86.206
$4s5p\ ^3P_1$	0.00031	88.069	−0.027
Remainder	4.919	8.813	9.388
α_{core}	3.166	3.197	3.198
Total	0	0	0

It can be seen that a finite number of lower-level transitions dominate the contributions, as highlighted in bold in Table V. High-precision measurements of these magic-zero wavelengths are recommended to determine the corresponding oscillator strengths.

First, we recommend that the measurement of the 436-nm magic-zero wavelength can be used to determine the ratio of $f_{4s4p\ ^3P_0\to 4s4d\ ^3D_1}/f_{4s4p\ ^3P_0\to 4p^2\ ^3P_1}$. As can be seen in Table V, the dynamic polarizability is largely offset by these two transitions at this magic-zero wavelength. Consequently, the dynamic polarizability can be expressed as

$$0=\frac{f_{4s4p\ ^3P_0\to 4s4d\ ^3D_1}}{\varepsilon^2_{4s4p\ ^3P_0\to 4s4d\ ^3D_1}-\omega^2}+\frac{f_{4s4p\ ^3P_0\to 4p^2\ ^3P_1}}{\varepsilon^2_{4s4p\ ^3P_0\to 4p^2\ ^3P_1}-\omega^2}+\alpha_{\rm rem}(\omega), \tag{15}$$

where $\alpha_{\rm rem}(\omega)$ denotes the contribution from the remainder transitions except the $4s4p\ ^3P_0\to 4s4d\ ^3D_1$ and $4s4p\ ^3P_0\to 4p^2\ ^3P_1$ transitions. By combining with the recent experimental value of the oscillator strength $f_{4s4p\ ^3P_0\to 4p^2\ ^3P_1}$ [60] listed in Table II, the ratio of $f_{4s4p\ ^3P_0\to 4s4d\ ^3D_1}/f_{4s4p\ ^3P_0\to 4p^2\ ^3P_1}$ can be determined using the measured magic-zero wavelength near 436 nm. If the uncertainty of the measured magic-zero wavelength is at a level of 0.001 nm, then the uncertainty of this ratio determined by Eq. (15) is about 0.1%. The porlarizabilities at the 576- and 436-nm magic-zero wavelengths are dominated by three transitions, i.e., $4s4p\ ^3P_0\to 4s5s\ ^3S_1$, $4s4p\ ^3P_0\to 4s4d\ ^3D_1$, and $4s4p\ ^3P_0\to 4p^2\ ^3P_1$. By combining the experimental value of $f_{4s4p\ ^3P_0\to 4s5s\ ^3S_1}$ [60] with measurements of these two magic-zero wavelengths, the values of $f_{4s4p\ ^3P_0\to 4s4d\ ^3D_1}$ and $f_{4s4p\ ^3P_0\to 4p^2\ ^3P_1}$ can be determined. If the uncertainty of the measured magic-zero wavelength is at a level of 0.001 nm, the final uncertainties of $f_{4s4p\ ^3P_0\to 4s4d\ ^3D_1}$ and $f_{4s4p\ ^3P_0\to 4p^2\ ^3P_1}$ will not exceed 1%, which is mainly caused by the uncertainties of $\alpha^{\rm rem}_{575}(\omega)$, $\alpha^{\rm rem}_{436}(\omega)$, and the oscillator strength $f_{4s4p\ ^3P_0\to 4s5s\ ^3S_1}$.

The dynamic polarizability at the 1414-nm magic-zero wavelength is dominated by the first four transitions. Except for the first transition $4s4p\ ^3P_0\to 3d4s\ ^3D_1$, the matrix elements for the other three transitions can be found in the NIST tabulations, as shown in Table II. Therefore, by combining these tabulations, the measurement of this magic-zero wavelength can be used to determine the matrix element of the $4s4p\ ^3P_0\to 3d4s\ ^3D_1$ transition. The accuracy of the determined matrix elements should be the same as that of the NIST tabulations. However, to obtain more accurate results, we recommend extracting these matrix elements by jointly measuring the 1414, 576, and 436 nm magic-zero wavelengths. With this method, the matrix elements of $4s4p\ ^3P_0\to 3d4s\ ^3D_1$, $4s4p\ ^3P_0\to 4s5s\ ^3S_1$, $4s4p\ ^3P_0\to 4s4d\ ^3D_1$, and $4s4p\ ^3P_0\to 4p2\ ^3P_1$ can be determined at the same time, and the accuracy could be significantly improved. Furthermore, if the remaining seven magic-zero wavelengths can be measured one by one, the remaining seven oscillator strengths can be extracted successively.

Table VI lists ten magic wavelengths in the range of 315 to 1500 nm for the $4s^2\ ^1S_0\to 4s4p\ ^3P_0$ transition, as well as the contributions to the dynamic polarizabilities. It is worth noting that the present magic wavelength of 736(10) nm agrees very well with the predicted value of 735.5(20) nm from Ref. [42], where the polarizability was derived from experimentally measured transition wavelengths and line strengths. However, the results calculated by Santra *et al.* using the one-particle model potential and finite-element basis method,

TABLE V. Magic-zero wavelengths (in nm) and the breakdowns of contributions (in a.u.) to the dynamic polarizabilities of the $4s4p\ ^3P_0$ state of Ca atoms. The first 11 rows give the contributions from the transitions indicated. "Remainder" is the contributions from all other transitions. The dominant contributions relevant to extracting the matrix elements are highlighted in bold.

λ_{zero}	1414(12)	576(1)	436.296(4)	395.824(32)	369.96(26)	347.38(4)	338.13(17)	327.24(5)	322.93(5)	316.73(3)
$3d4s\ ^3D_1$	**−157.49**	−13.28	−7.32	−5.97	−5.18	−4.55	−4.31	−4.02	−3.91	−3.76
$4s5s\ ^3S_1$	**34.24**	**−225.06**	−29.11	−20.22	−16.20	−13.35	−12.36	−11.24	−10.80	−10.26
$4s4d\ ^3D_1$	**43.90**	**96.84**	**−1346.82**	−158.02	−92.00	−63.52	−55.68	−47.71	−44.86	−41.52
$4p^2\ ^3P_1$	**47.51**	**97.00**	**1310.80**	−246.63	−125.46	−82.13	−70.99	−60.04	−56.11	−51.63
$4s6s\ ^3S_1$	1.52	2.64	7.76	**336.27**	−9.83	−4.77	−3.86	−3.06	−2.80	−2.52
$4s5d\ ^3D_1$	7.86	12.17	23.73	45.57	**184.32**	−82.69	−49.75	−32.31	−27.96	−23.67
$4s7s\ ^3S_1$	0.41	0.60	1.04	1.65	3.16	**152.34**	−7.48	−3.08	−2.53	−1.91
$4s6d\ ^3D_1$	2.86	4.08	6.56	9.46	14.77	37.19	**128.26**	−60.24	−38.33	−20.60
$4s8s\ ^3S_1$	0.17	0.24	0.38	0.52	0.76	1.45	2.63	**111.50**	−7.24	−2.48
$4s7d\ ^3D_1$	1.21	1.66	2.50	3.35	4.67	7.88	11.66	30.93	**100.67**	−43.05
$4s9s\ ^3S_1$	0.09	0.13	0.19	0.25	0.33	0.53	0.71	1.38	2.14	**78.71**
Remainder	17.72	22.98	30.29	33.77	40.66	51.62	61.17	77.89	91.73	122.69
Total	0	0	0	0	0	0	0	0	0	0

TABLE VI. Magic wavelengths (in nm) for the $4s^2\ ^1S_0 \rightarrow 4s4p\ ^3P_0$ transition and the breakdown of contributions to the dynamic polarizabilities (a.u.) of the $4s^2\ ^1S_0$ and $4s4p\ ^3P_0$ states. The dominant contributions relevant to extracting the matrix elements are highlighted in bold.

λ_{magic}	736(10)	657.49(1)	456.10(2)	431.06(1)	394.60(1)	357.44(3)	346.52(2)	331.56(6)	326.76(1)	319.63(3)
Expt.	735.5(20) [42]									
					$4s^2\ ^1S_0$					
$4s4p\ ^1P_1$	224.20	256.49	1067.59	3956.11	−1016.60	−376.91	−307.97	−241.17	−223.26	−201.45
$4s4p\ ^3P_1$	0.05	108.99	−1.04	−8.45	−6.31	−4.71	−0.004	−0.003	−0.004	−0.003
$3d4p\ ^1P_1$	1.97	2.02	2.38	2.48	2.69	3.02	3.17	3.41	3.51	3.67
$4s6p\ ^1P_1$	1.73	1.79	2.14	2.24	2.46	2.82	2.97	3.25	3.36	3.54
Remainder	2.56	2.61	3.93	10.66	9.44	8.10	3.50	3.65	3.73	3.82
Total	230.51	371.90	1075.00	3963.81	−1008.32	−367.68	−298.33	−230.86	−212.66	−190.42
					$4s4p\ ^3P_0$					
$3d4s\ ^3D_1$	−23.17	−17.86	−8.05	−7.14	−5.94	−4.83	−4.53	−4.14	−4.01	−3.84
$4s5s\ ^3S_1$	**89.42**	**201.95**	−35.23	−27.72	−20.00	−14.54	−13.25	−11.69	−11.19	−10.55
$4s4d\ ^3D_1$	62.07	72.49	**681.35**	**−725.81**	−153.25	−74.22	−62.70	−50.78	−47.44	−43.29
$4p^2\ ^3P_1$	65.27	75.15	**374.41**	**4651.07**	−236.71	−97.87	−80.96	−64.18	−59.61	−54.01
$4s6s\ ^3S_1$	2.00	2.23	5.69	8.72	**−688.98**	−6.32	−4.67	−3.35	−3.03	−2.67
$4s5d\ ^3D_1$	9.69	10.56	19.95	25.10	47.71	**−250.94**	−80.92	−37.93	−31.87	−25.86
$4s7s\ ^3S_1$	0.49	0.53	0.91	1.09	1.69	6.63	**−156.46**	−4.10	−3.02	−2.18
$4s6d\ ^3D_1$	3.41	3.66	5.85	6.75	9.61	21.90	39.72	**−149.31**	−56.27	−28.84
$4s8s\ ^3S_1$	0.21	0.22	0.34	0.39	0.53	1.01	1.50	5.74	**−110.24**	−3.66
$4s7d\ ^3D_1$	1.41	1.50	2.27	2.57	3.39	5.94	8.10	18.05	33.11	**−125.15**
Remainder	19.71	21.47	27.51	28.79	33.63	45.56	52.84	70.82	80.91	109.63
Total	230.51	371.90	1075.00	3963.81	−1008.32	−367.68	−298.33	−230.86	−212.66	−190.42

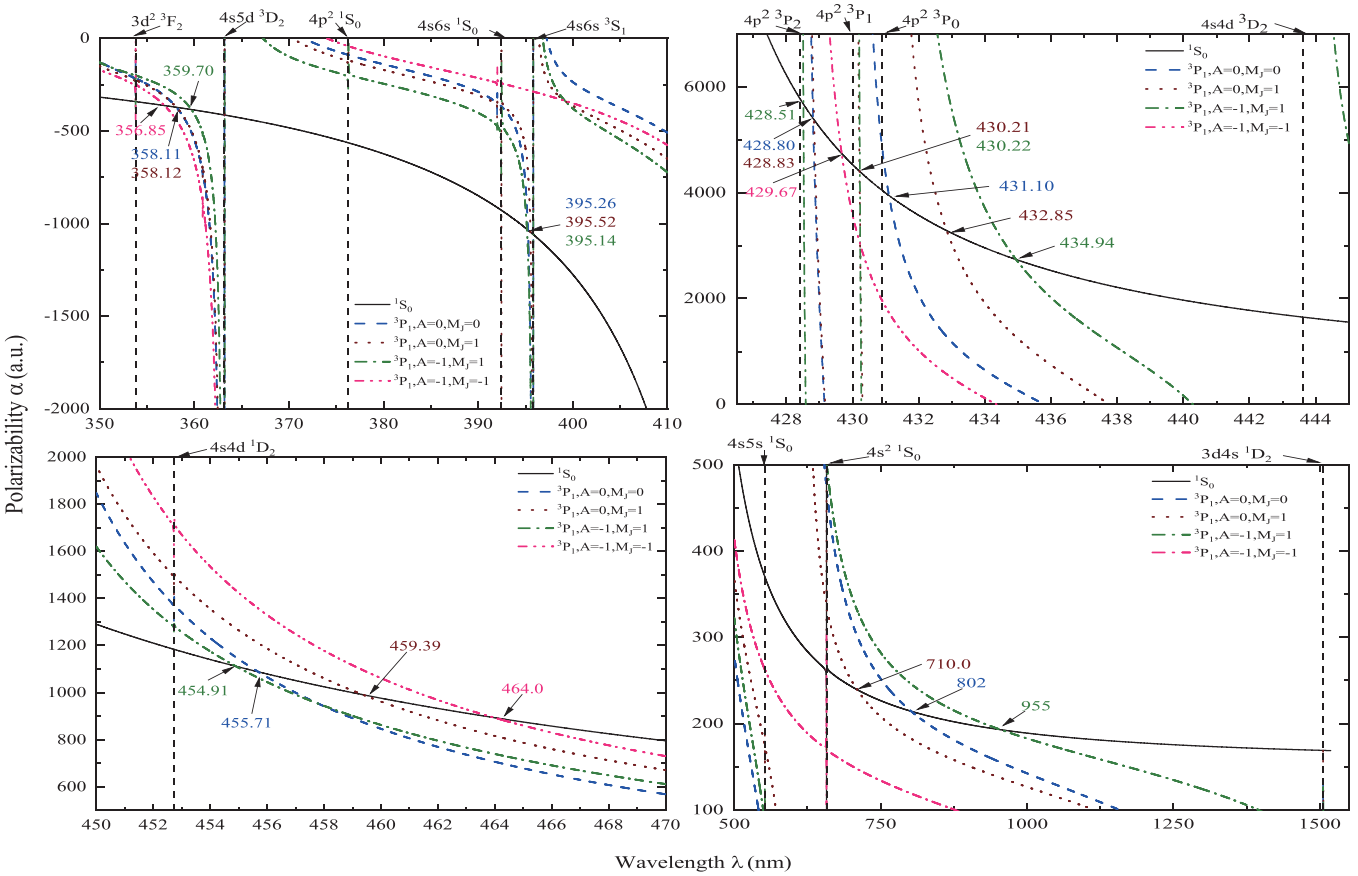

FIG. 2. The dynamical polarizabilities of $^1S_0$ and $^3P_1$ states. The vertical dashed lines indicate the position of the resonant transition. The upper states for resonances from the $4s4p\ ^3P_1$ state are given on the top of the figures, and the magic wavelengths are determined by locating points where the $4s4p\ ^3P_1$ and $4s^2\ ^1S_0$ polarizabilities are equal to each other. They are all identified by arrows in this figure.

TABLE VII. Magic wavelengths (in nm) for the $4s^2\ ^1S_0 \rightarrow 4s4p\ ^3P_1$ transition of Ca atoms in the case of the magnetic field being parallel to the wave vector $\hat{k}$, that is $\cos\theta_k = 1$.

		$\mathcal{A}=0$			$\mathcal{A}=-1$		
		$M_J=0$		$M_J=1$	$M_J=1$		$M_J=-1$
Resonances	λ_{res} (nm)	Present	Refs.	Present	Present	Refs.	Present
$4s4p\ ^3P_1 \rightarrow 3d4s\ ^1D_2$	1506.12						
			799.2[a] [46]	710.0(8.7)	955(24)	983(12)[a] [42]	
		802(11)	800.8(22)[b] [42]				
			799.17[a] [48]				
$4s4p\ ^3P_1 \rightarrow 4s^2\ ^1S_0$	657.46						
$4s4p\ ^3P_1 \rightarrow 4s5s\ ^1S_0$	552.27						
		455.71(2)	456.20[a] [48]	459.39(67)	454.91(44)		464.0(2.2)
$4s4p\ ^3P_1 \rightarrow 4s4d\ ^1D_2$	452.73						
$4s4p\ ^3P_1 \rightarrow 4s4d\ ^3D_2$	443.62						
		431.10(1)	431.10[a] [48]	432.85(7)	434.94(2)		
$4s4p\ ^3P_1 \rightarrow 4p^2\ ^3P_0$	430.90						
				430.21(2)	430.22(2)		
$4s4p\ ^3P_1 \rightarrow 4p^2\ ^3P_1$	430.02						
		428.80(1)	428.82[a] [48]	428.83(2)	428.51(1)		429.67(5)
$4s4p\ ^3P_1 \rightarrow 4p^2\ ^3P_1$	428.42						
$4s4p\ ^3P_1 \rightarrow 4s6s\ ^3S_1$	395.82						
		395.26(1)		395.52(1)	395.14(2)		
$4s4p\ ^3P_1 \rightarrow 4s6s\ ^1S_0$	392.46						
$4s4p\ ^3P_1 \rightarrow 4s5d\ ^3D_2$	363.18						
		358.11(15)		358.12(2)	359.70(9)		356.85(26)
$4s4p\ ^3P_1 \rightarrow 3d^2\ ^3F_2$	353.80						

[a]Theoretical value.
[b]Experimental value.

700 nm [95], are quite different from our results and the predictions of Degenhardt *et al.* [42]. It can be seen from this table that the breakdowns are similar to those at the magic-zero wavelengths; i.e., a finite number of lower-level transitions dominate the contributions. Measuring these magic wavelengths can further enable the extraction of oscillator strengths. For example, the values of $f_{4s4p\ ^3P_0 \rightarrow 4s4d\ ^3D_1}$ and $f_{4s4p\ ^3P_0 \rightarrow 4p^2\ ^3P_1}$ can be determined by measuring the 456- and 431-nm magic wavelengths, respectively.

D. The magic wavelengths for the $4s^2\ ^1S_0 \rightarrow 4s4p\ ^3P_1$ transition

The ultranarrow-bandwidth $4s^2\ ^1S_0 \rightarrow 4s4p\ ^3P_1$ intercombination transition is of great interest in the technologies of optical frequency metrology, the generation of a BEC, and the superradiant lasers [38,40,45]. For the $4s4p\ ^3P_1$ state, the dynamic polarizability is associated with the magnetic quantum number m_{j_i}, the degree of polarization $\mathcal{A}$, and the angles θ_k and θ_p, as illustrated in Eq. (8).

When the magnetic field is parallel to the wave vector $\hat{k}$, that is, $\cos\theta_k = 1$ and $\cos^2\theta_p = 0$. Figure 2 shows the dynamic polarizabilities of the ground state and each of the magnetic sublevels of the $4s4p\ ^3P_1$ states with $\mathcal{A}=0$ and -1. The magic wavelengths are identified with arrows. Table VII lists these magic wavelengths and compares with other available results. For linearly polarized light (i.e., $\mathcal{A}=0$), the longest magic wavelength of $M_J=0$ magnetic sublevel transitions, 802(11) nm, agrees well with the experimental result of 800.8(22) nm [42] and the calculations of Refs. [46,48]. Our magic wavelengths of 455.71, 431.10, and 428.80 nm are in good agreement with the results of Ref. [48], with differences of no more than 0.2%. Seven magic wavelengths are found for the $M_J=1$ transition, and there are no other results available for this transition. For the left-handed circularly polarized light (i.e., $\mathcal{A}=-1$), the polarizabilities of the $M_J=0$ magnetic sublevel are the same as those for the $\mathcal{A}=0$ case. Therefore, in Table VI, we only list the magic wavelengths for the $M_J=1$ and -1 transitions for the case of $\mathcal{A}=-1$. The presently calculated longest magic wavelength for the $M_J=1$ magnetic sublevel transition, 955 nm, is in good agreement with the predicted result of 983(12) nm [42], with the difference being less than 3%. Three magic wavelengths are found for the $M_J=-1$ sublevel transition.

When the magnetic field is perpendicular to the wave vector $\hat{k}$, i.e., $\cos\theta_k = 0$, the dynamic polarizability and the determination of magic wavelengths only depend on $\cos^2\theta_p$, as given in Eq. (14). Note that for linearly polarized light, θ_p is the angle between the direction of polarization and the magnetic field (quantization axis $\hat{e}_z$). For a given $\mathcal{A}$, $\cos^2\theta_p$ satisfies

$$\frac{1}{2} - \frac{\sqrt{1-\mathcal{A}^2}}{2} \leqslant \cos^2\theta_p \leqslant \frac{1}{2} + \frac{\sqrt{1-\mathcal{A}^2}}{2}. \tag{16}$$

Figure 3 shows the dependence of the magic wavelengths upon $\cos\theta_p$. Based on the sensitivity of the magic wavelengths to $\cos\theta_p$, they can be separated into three groups. The first group includes the magic wavelengths near 800 nm, which lie between the transition wavelengths of $4s4p\ ^3P_1 \rightarrow$

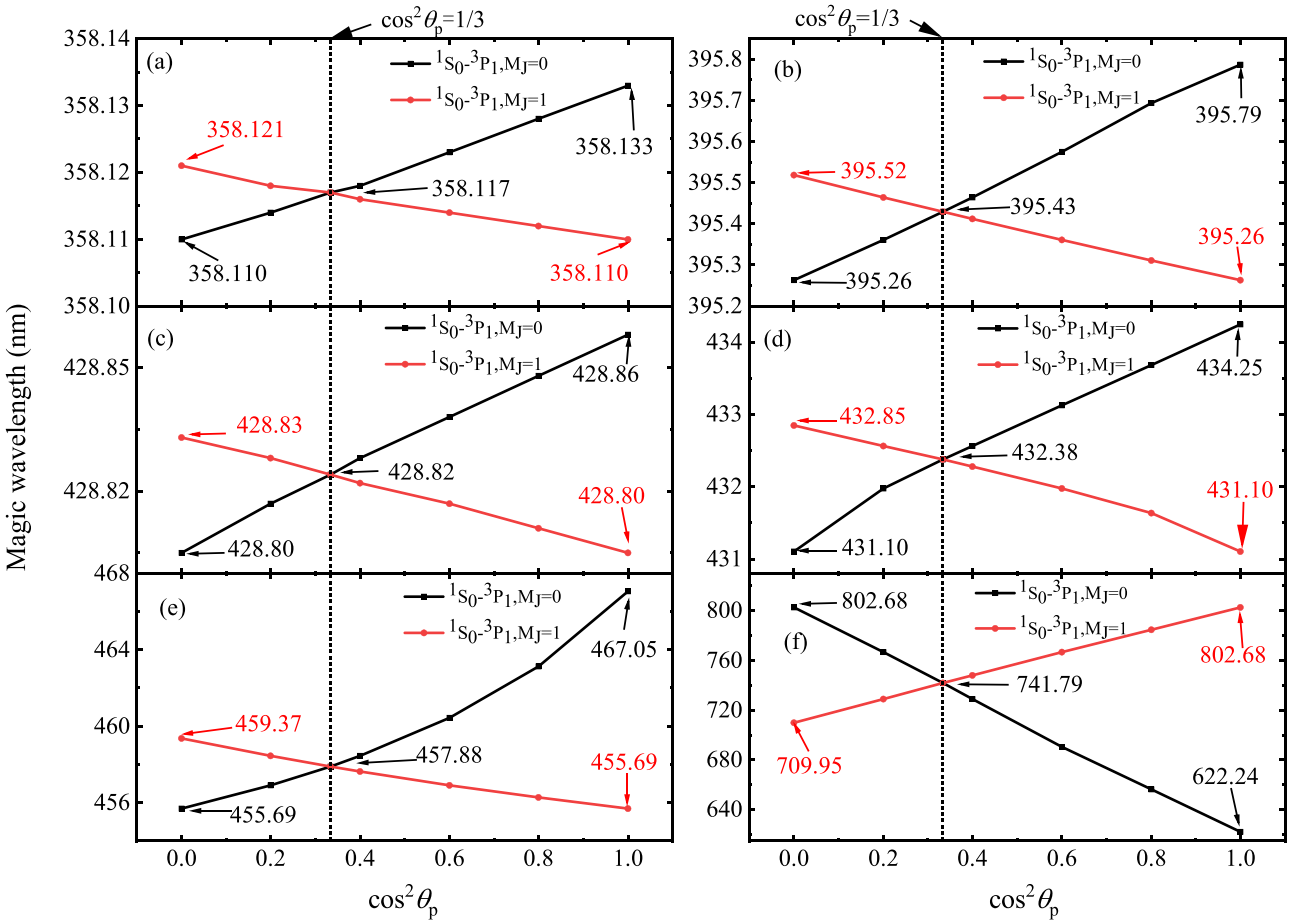

FIG. 3. The dependence of magic wavelengths of each of the magnetic sublevel transitions on $\cos\theta_p$ in the case of the magnetic field being perpendicular to the wave vector $\hat{k}$, i.e., $\cos\theta_k = 0$.

$3d4s\ ^1D_2$ and $4s4p\ ^3P_1 \rightarrow 4s^2\ ^1S_0$. These magic wavelengths are very sensitive to $\cos\theta_p$, varying significantly with changes in $\cos\theta_p$. The second group includes the magic wavelengths near 455 and 431 nm, which are less sensitive than the first group. For example, the difference in the magic wavelengths near 459 nm of the $^1S_0 \rightarrow {}^3P_1$, $M_J = 1$, transition is only about 4 nm for $\cos^2\theta_p = 0$ and $\cos^2\theta_p = 1$. The third group includes those near 428, 395, and 358 nm, which are insensitive to the $\cos\theta_p$. As $\cos\theta_p$ varies, the change in these magic wavelengths is within the range of 0.5 nm. It can also be found in this figure that when $\cos^2\theta_p = 1/3$, which is related to the magic angle [96], the magic wavelengths become independent of the magnetic sublevels.

IV. CONCLUSIONS

Using the RCI + MBPT method, we have calculated the energy levels, the reduced $E1$ transition matrix elements, and the polarizabilities of the $4s^2\ ^1S_0$, $4s4p\ ^1P_1$, and $4s4p\ ^3P_{1,2}$ states of Ca atoms. Our results show good agreement with experimental and other theoretical results.

Ten magic-zero wavelengths of the $4s4p\ ^3P_0$ state and ten magic wavelengths of the $4s^2\ ^1S_0 \rightarrow 4s4p\ ^3P_0$ transition ranging from 315 to 1500 nm are identified. Since a finite number of lower-level transitions dominate the contributions of the polarizabilities at magic-zero wavelengths, we propose a method for extracting the oscillator strengths using precise measurements of the magic-zero wavelengths of the $4s4p\ ^3P_0$ state. The ratio of $f_{4s4p\ ^3P_0\rightarrow 4s4d\ ^3D_1}/f_{4s4p\ ^3P_0\rightarrow 4p^2\ ^3P_1}$ can be determined by measuring the 436-nm magic-zero wavelength. By combining the measurements of the 576- and 436-nm magic-zero wavelengths with the recent experimental value of the oscillator strength of $f_{4s4p\ ^3P_0\rightarrow 4s5s\ ^3S_1}$ [60], the values of $f_{4s4p\ ^3P_0\rightarrow 4s4d\ ^3D_1}$ and $f_{4s4p\ ^3P_0\rightarrow 4p^2\ ^3P_1}$ can be determined. If the magic-zero wavelengths can be measured one by one, the transition oscillator strengths from the $4s4p\ ^3P_0$ state to higher excited states can be extracted successively. Similarly, the oscillator strength can also be extracted by measuring the magic wavelength of the $4s^2\ ^1S_0 \rightarrow 4s4p\ ^3P_0$ transition. For example, $f_{4s4p\ ^3P_0\rightarrow 4s4d\ ^3D_1}$ and $f_{4s4p\ ^3P_0\rightarrow 4p^2\ ^3P_1}$ can be determined by measuring the 456- and 431-nm magic wavelengths.

In addition, the magic wavelengths of the $4s^2\ ^1S_0 \rightarrow 4s4p\ ^3P_1$ transition are identified. These magic wavelengths depend on the degree of polarization $\mathcal{A}$ and the angles of θ_k and θ_p. When the magnetic field is parallel to the wave vector $\hat{k}$, our results agree well with some available experimental results [42] and predictions [46,48]. When the magnetic field is perpendicular to the wave vector $\hat{k}$, the magic wavelength is related to the polarization angle θ_p. The dependence of the magic wavelengths on $\cos^2\theta_p$ is analyzed. We found that the magic wavelengths near 802, 455, and 431 nm are sensitive to $\cos^2\theta_p$. However, the magic wavelengths near 428, 395,

and 358 nm are insensitive to $\cos^2\theta_p$, and the variation of the magic wavelengths is in the range of 0.5 nm.

ACKNOWLEDGMENTS

We thank Prof. T. Shi and Dr. Y. Cheng for helpful discussions. This work has been supported by the National Key Research and Development Program of China under Grant No. 2022YFA1602500, the National Natural Science Foundation of China under Grants No. 12174316 and No. 12174268, the Innovative Fundamental Research Group Project of Gansu Province (Grant No. 20JR5RA541), and the project of the Educational Commission of Guangdong Province of China (Grant No. 2020KTSCX124).

[1] E. Pedrozo-Peñafiel, S. Colombo, C. Shu, A. F. Adiyatullin, Z. Li, E. Mendez, B. Braverman, A. Kawasaki, D. Akamatsu, Y. Xiao *et al.*, Nature (London) **588**, 414 (2020).
[2] A. W. Young, W. J. Eckner, W. R. Milner, D. Kedar, M. A. Norcia, E. Oelker, N. Schine, J. Ye, and A. M. Kaufman, Nature (London) **588**, 408 (2020).
[3] E. Oelker, R. Hutson, C. Kennedy, L. Sonderhouse, T. Bothwell, A. Goban, D. Kedar, C. Sanner, J. Robinson, G. Marti *et al.*, Nat. Photonics **13**, 714 (2019).
[4] M. A. Norcia, A. W. Young, W. J. Eckner, E. Oelker, J. Ye, and A. M. Kaufman, Science **366**, 93 (2019).
[5] B. J. Bloom, T. L. Nicholson, J. R. Williams, S. L. Campbell, M. Bishof, X. Zhang, W. Zhang, S. L. Bromley, and J. Ye, Nature (London) **506**, 71 (2014).
[6] R. Li, F. N. Baynes, A. N. Luiten, and C. Perrella, Phys. Rev. Appl. **14**, 064067 (2020).
[7] J. Kong, R. Jiménez-Martínez, C. Troullinou, V. G. Lucivero, G. Tóth, and M. W. Mitchell, Nat. Commun. **11**, 1 (2020).
[8] F. Schreck and K. van Druten, Nat. Phys. **17**, 1296 (2021).
[9] S. S. Szigeti, O. Hosten, and S. A. Haine, Appl. Phys. Lett. **118**, 140501 (2021).
[10] A. Belenchia, M. Carlesso, Ö. Bayraktar, D. Dequal, I. Derkach, G. Gasbarri, W. Herr, Y. L. Li, M. Rademacher, J. Sidhu *et al.*, Phys. Rep. **951**, 1 (2022).
[11] G. Biedermann, X. Wu, L. Deslauriers, S. Roy, C. Mahadeswaraswamy, and M. Kasevich, Phys. Rev. A **91**, 033629 (2015).
[12] M. D. Gregoire, I. Hromada, W. F. Holmgren, R. Trubko, and A. D. Cronin, Phys. Rev. A **92**, 052513 (2015).
[13] J. Ye, D. W. Vernooy, and H. J. Kimble, Phys. Rev. Lett. **83**, 4987 (1999).
[14] H. Katori, T. Ido, and M. Kuwata-Gonokami, J. Phys. Soc. Jpn. **68**, 2479 (1999).
[15] C. D. Herold, V. D. Vaidya, X. Li, S. L. Rolston, J. V. Porto, and M. S. Safronova, Phys. Rev. Lett. **109**, 243003 (2012).
[16] R. H. Leonard, A. J. Fallon, C. A. Sackett, and M. S. Safronova, Phys. Rev. A **92**, 052501 (2015).
[17] W. F. Holmgren, R. Trubko, I. Hromada, and A. D. Cronin, Phys. Rev. Lett. **109**, 243004 (2012).
[18] R. Trubko, M. D. Gregoire, W. F. Holmgren, and A. D. Cronin, Phys. Rev. A **95**, 052507 (2017).
[19] M. S. Safronova, Z. Zuhrianda, U. I. Safronova, and C. W. Clark, Phys. Rev. A **92**, 040501(R) (2015).
[20] J. Jiang, L. Y. Tang, and J. Mitroy, Phys. Rev. A **87**, 032518 (2013).
[21] L. Morel, Z. Yao, P. Cladé, and S. Guellati-Khélifa, Nature (London) **588**, 61 (2020).
[22] Boulder Atomic Clock Optical Network (BACON) Collaboration, Nature (London) **591**, 564 (2021).
[23] B. Henson, J. Ross, K. Thomas, C. Kuhn, D. Shin, S. Hodgman, Y. H. Zhang, L. Y. Tang, G. Drake, A. Bondy *et al.*, Science **376**, 199 (2022).
[24] B. M. Henson, R. I. Khakimov, R. G. Dall, K. G. H. Baldwin, L. Y. Tang, and A. G. Truscott, Phys. Rev. Lett. **115**, 043004 (2015).
[25] A. Ratkata, P. D. Gregory, A. D. Innes, A. J. Matthies, L. A. McArd, J. M. Mortlock, M. S. Safronova, S. L. Bromley, and S. L. Cornish, Phys. Rev. A **104**, 052813 (2021).
[26] A. M. Kaufman and K.-K. Ni, Nat. Phys. **17**, 1324 (2021).
[27] P. Halder, H. Winter, and A. Hemmerich, Phys. Rev. A **88**, 063639 (2013).
[28] T. Köhler, K. Góral, and P. S. Julienne, Rev. Mod. Phys. **78**, 1311 (2006).
[29] A. Derevianko, S. G. Porsev, S. Kotochigova, E. Tiesinga, and P. S. Julienne, Phys. Rev. Lett. **90**, 063002 (2003).
[30] U. Dammalapati, I. Norris, L. Maguire, M. Borkowski, and E. Riis, Meas. Sci. Technol. **20**, 095303 (2009).
[31] O. Appel, Ph.D. thesis, Gottfried Wilhelm Leibniz Universität Hannover, Hannover, 2014.
[32] J. Grünert and A. Hemmerich, Phys. Rev. A **65**, 041401(R) (2002).
[33] P. Halder, C. Y. Yang, and A. Hemmerich, Phys. Rev. A **85**, 031603(R) (2012).
[34] D. Hansen and A. Hemmerich, Phys. Rev. Lett. **96**, 073003 (2006).
[35] B. Bussery-Honvault, J.-M. Launay, and R. Moszynski, Phys. Rev. A **68**, 032718 (2003).
[36] D. P. Hansen, J. R. Mohr, and A. Hemmerich, Phys. Rev. A **67**, 021401(R) (2003).
[37] F. Vogt, C. Grain, T. Nazarova, U. Sterr, F. Riehle, C. Lisdat, and E. Tiemann, Eur. Phys. J. D **44**, 73 (2007).
[38] S. Kraft, F. Vogt, O. Appel, F. Riehle, and U. Sterr, Phys. Rev. Lett. **103**, 130401 (2009).
[39] A. Derevianko and H. Katori, Rev. Mod. Phys. **83**, 331 (2011).
[40] A. D. Ludlow, M. M. Boyd, J. Ye, E. Peik, and P. O. Schmidt, Rev. Mod. Phys. **87**, 637 (2015).
[41] T. Fortier and E. Baumann, Commun. Phys. **2**, 153 (2019).
[42] C. Degenhardt, H. Stoehr, U. Sterr, F. Riehle, and C. Lisdat, Phys. Rev. A **70**, 023414 (2004).
[43] C. Degenhardt, H. Stoehr, C. Lisdat, G. Wilpers, H. Schnatz, B. Lipphardt, T. Nazarova, P.-E. Pottie, U. Sterr, J. Helmcke *et al.*, Phys. Rev. A **72**, 062111 (2005).
[44] G. Wilpers, C. Degenhardt, T. Binnewies, A. Chernyshov, F. Riehle, J. Helmcke, and U. Sterr, Appl. Phys. B **76**, 149 (2003).
[45] T. Laske, H. Winter, and A. Hemmerich, Phys. Rev. Lett. **123**, 103601 (2019).
[46] X. Zhou, X. Xu, X. Chen, and J. Chen, Phys. Rev. A **81**, 012115 (2010).

[47] A. Kramida, Yu. Ralchenko, J. Reader, and NIST ASD Team, NIST Atomic Spectra Database (version 5.10) [online], available at https://physics.nist.gov/asd [2022, October 12] (National Institute of Standards and Technology, Gaithersburg, MD, 2022).

[48] A. Gogyan, G. Kazakov, M. Bober, and M. Zawada, Opt. Express **28**, 6881 (2020).

[49] Y. Cheng, J. Jiang, and J. Mitroy, Phys. Rev. A **88**, 022511 (2013).

[50] S. G. Porsev, M. G. Kozlov, Y. G. Rakhlina, and A. Derevianko, Phys. Rev. A **64**, 012508 (2001).

[51] C. F. Fischer and G. Tachiev, Phys. Rev. A **68**, 012507 (2003).

[52] G. Zinner, T. Binnewies, F. Riehle, and E. Tiemann, Phys. Rev. Lett. **85**, 2292 (2000).

[53] I. M. Savukov and W. R. Johnson, Phys. Rev. A **65**, 042503 (2002).

[54] F. Kelly and M. Mathur, Can. J. Phys. **58**, 1416 (1980).

[55] S. G. Porsev and A. Derevianko, Phys. Rev. A **65**, 020701(R) (2002).

[56] W. Hansen, J. Phys. B **16**, 2309 (1983).

[57] D. Husain, J. Chem. Soc., Faraday Trans. 2 **85**, 85 (1989).

[58] R. Drozdowski, M. Ignaciuk, J. Kwela, and J. Heldt, Z. Phys. D **41**, 125 (1997).

[59] P. Whitkop and J. Wiesenfeld, Chem. Phys. Lett. **69**, 457 (1980).

[60] E. Den Hartog, J. Lawler, C. Sneden, J. Cowan, I. Roederer, and J. Sobeck, Astrophys. J., Suppl. Ser. **255**, 27 (2021).

[61] V. A. Dzuba, V. V. Flambaum, and M. G. Kozlov, Phys. Rev. A **54**, 3948 (1996).

[62] V. A. Dzuba and W. R. Johnson, Phys. Rev. A **57**, 2459 (1998).

[63] M. G. Kozlov, S. G. Porsev, M. S. Safronova, and I. I. Tupitsyn, Comput. Phys. Commun. **195**, 199 (2015).

[64] V. A. Dzuba, Phys. Rev. A **71**, 032512 (2005).

[65] M. S. Safronova, M. G. Kozlov, W. R. Johnson, and D. Jiang, Phys. Rev. A **80**, 012516 (2009).

[66] V. A. Dzuba, V. V. Flambaum, M. G. Kozlov, and S. G. Porsev, J. Exp. Theor. Phys. **87**, 885 (1998).

[67] I. M. Savukov and W. R. Johnson, Phys. Rev. A **62**, 052512 (2000).

[68] Y. B. Tang, H. X. Qiao, T. Y. Shi, and J. Mitroy, Phys. Rev. A **87**, 042517 (2013).

[69] Y. B. Tang, C. B. Li, and H. X. Qiao, Chin. Phys. B **23**, 063101 (2014).

[70] Y. B. Tang, B. Q. Lou, and T. Y. Shi, Phys. Rev. A **96**, 022513 (2017).

[71] M. S. Safronova and U. I. Safronova, Phys. Rev. A **83**, 012503 (2011).

[72] E. F. Archibong and A. J. Thakkar, Phys. Rev. A **44**, 5478 (1991).

[73] S. Jackson and A. C. Vutha, Phys. Rev. A **99**, 063422 (2019).

[74] W. Müller, J. Flesch, and W. Meyer, J. Chem. Phys. **80**, 3297 (1984).

[75] J. Mitroy and M. W. J. Bromley, Phys. Rev. A **68**, 052714 (2003).

[76] I. S. Lim and P. Schwerdtfeger, Phys. Rev. A **70**, 062501 (2004).

[77] S. Porsev and A. Derevianko, J. Exp. Theor. Phys. **102**, 195 (2006).

[78] J. Mitroy and J. Y. Zhang, J. Chem. Phys. **128**, 134305 (2008).

[79] T. M. Miller, in *CRC Handbook of Chemistry and Physics*, 77th ed., edited by D. R. Lide (CRC, Boca Raton, FL, 2000), p. 193.

[80] R. W. Molof, H. L. Schwartz, T. M. Miller, and B. Bederson, Phys. Rev. A **10**, 1131 (1974).

[81] S. G. Porsev and A. Derevianko, Phys. Rev. A **74**, 020502(R) (2006).

[82] M. Mérawa, C. Tendero, and M. Rerat, Chem. Phys. Lett. **343**, 397 (2001).

[83] A. Kreutzträger and G. Oppen, Z. Phys. **265**, 421 (1973).

[84] G. von Oppen, Z. Phys. A: Hadrons Nucl. **232**, 473 (1970).

[85] S. Yanagimachi, M. Kajiro, M. Machiya, and A. Morinaga, Phys. Rev. A **65**, 042104 (2002).

[86] K. Zeiske, G. Zinner, F. Riehle, and J. Helmcke, Appl. Phys. B **60**, 205 (1995).

[87] N. L. Manakov, V. D. Ovsiannikov, and L. P. Rapoport, Phys. Rep. **141**, 320 (1986).

[88] K. Beloy, thesis, University of Nevada, Reno, 2009.

[89] F. Le Kien, P. Schneeweiss, and A. Rauschenbeutel, Eur. Phys. J. D **67**, 92 (2013).

[90] J. Mitroy, M. S. Safronova, and C. W. Clark, J. Phys. B **43**, 202001 (2010).

[91] J. Jiang, L. Jiang, Z. W. Wu, D. H. Zhang, L. Y. Xie, and C. Z. Dong, Phys. Rev. A **99**, 032510 (2019).

[92] J. Jiang, X. J. Li, X. Wang, C. Z. Dong, and Z. W. Wu, Phys. Rev. A **102**, 042823 (2020).

[93] R. Glass, J. Phys. B **20**, 4649 (1987).

[94] C. Degenhardt, T. Binnewies, G. Wilpers, U. Sterr, F. Riehle, C. Lisdat, and E. Tiemann, Phys. Rev. A **67**, 043408 (2003).

[95] R. Santra, K. V. Christ, and C. H. Greene, Phys. Rev. A **69**, 042510 (2004).

[96] D. Budker, D. Kimball, D. F. Kimball, and D. P. DeMille, *Atomic Physics: An Exploration through Problems and Solutions* (Oxford University, New York, 2004).